KAPL-P-000230
(K96114)

Analysis of Unclad and Sub-clad Semi-elliptical Flaws in Pressure Vessel Steels

H. Irizarry-Quinones, B. D. Macdonald, et. al.

September 1996

NOTICE

KAPL ATOMIC POWER LABORATORY SCHENECTADY, NEW YORK 12301

Operated for the U. S. Department of Energy
by KAPL, Inc. a Lockheed Martin company

DISCLAIMER

DISCLAIMER

Portions of this document may be illegible in electronic image products. Images are produced from the best available original document.

Hugo Irizarry-Quiñones[1], Bruce D. Macdonald[1], and Wallace J. McAfee[2]

ANALYSIS OF UNCLAD AND SUB-CLAD SEMI-ELLIPTICAL FLAWS IN PRESSURE VESSEL STEELS

REFERENCE: Irizarry-Quiñones, H., Macdonald, B.D., and McAfee, W.J., "**Analysis of Unclad and Sub-clad Semi-Elliptical Flaws in Pressure Vessel Steels**", Fatigue and Fracture Mechanics: 28th Volume, ASTM STP 1321, J.H. Underwood, B.D. Macdonald, and M.R. Mitchell, Eds., American Society for Testing and Materials, Philadelphia, 1997.

ABSTRACT: This study was conducted to support warm prestress experiments on unclad and sub-clad flawed beams loaded in pure bending. Two cladding yield strengths were investigated: 0.6 Sy and 0.8 Sy, where Sy is the yield strength of the base metal. Cladding and base metal were assumed to be stress free at the stress relief temperature for the 3D elastic-plastic finite element analysis. The model results indicated that when cooled from the stress relief temperature tensile residual stresses were generated in the cladding due to its greater coefficient of thermal expansion. The magnitude of the residual stresses depended on the amount of cooling and the strength of the cladding relative to that of the base metal. During loading, the sub-clad flaw elastic-plastic stress intensity factor, $K_I(J)$, was at first dominated by crack closing force due to tensile residual stresses in the cladding. After the cladding residual stress were overcome by the applied bending stresses, $K_I(J)$ gradually increased as if it were an unclad beam. A combination of elastic stress intensity factor solutions was used to approximate the effect of cladding in reducing the crack driving force along the flaw. This approximation was quite in keeping with the 3D elastic-plastic finite element solution for the sub-clad flaw.

Finally, a number of sub-clad flaw specimens not subjected to warm prestressing were thought to have suffered degraded toughness caused by locally intensified strain ageing embrittlement due to welding over the preexisting flaw.

KEYWORDS: Warm prestress, cladding, semi-elliptical flaws, sub-clad flaws, stress intensity factors, cladding residual stresses, locally intensified strain ageing embrittlement

---

The purpose of this study was to calculate stress intensity factors along the crack front of sub-clad and unclad four-point bend beams to support the interpretation of warm prestress (WPS) experiments. WPS is defined as an experimental observed phenomenon where a flawed component which was pre-loaded at a higher temperature experiences an enhancement of the fracture resistance at lower temperatures [1]. The WPS experiments

1. Lockheed Martin Corporation, PO Box 1072, Schenectady, NY 12309-1072
2. Oak Ridge National Laboratory, PO Box 2009, Oak Ridge, TN 37831-8056

were performed at Oak Ridge National Laboratory for Lockheed Martin Corporation [2]. Appendix A provides a summary of the experiments and a description of the specimens.

This paper describes the analyses performed to model the stress relieving process and the loading to failure. Stress intensity factors were obtained using finite element methods for different clad materials, test temperatures, and applied loads. The stress intensity factors were calculated using both linear-elastic and elastic-plastic fracture mechanics methods. Elastic-plastic fracture mechanics methods were used to model the stress relieving process applied to the WPS specimens after welding but prior to loading.

FINITE ELEMENT MODELING

As explained in Appendix A, the full beam configuration for the unclad WPS test specimens beams was 864 mm long, 102 mm high, and 127 mm wide. The full beam configuration was a composite design in which only the test section was fabricated from pedigreed material. The test section was 76 mm long, 102 mm high, and 127 mm wide. Test sections were taken from an ASTM A508 Class 2 steel pressure vessel cylinder. Reusable extension arms were electron-beam welded to the ends of the test section to form the full beam configuration.

The WPS specimen was modeled using quarter symmetry. Two finite element models were created using the PATRAN preprocessor [3]. Figure 1 shows the resulting unclad WPS specimen finite element model which was 432 mm long, 102 mm high, and 64 mm wide. Figure 2 shows a detail of the resulting clad WPS specimen finite element model which had an additional layer 6 mm thick to simulate the cladding.

The unclad WPS specimen finite element model had 626 elements and 3 188 nodes. The sub-clad WPS specimen finite element model had 922 elements and 4 543 nodes. The cladding was modeled using two planes of elements 3 mm thick each added to the top of

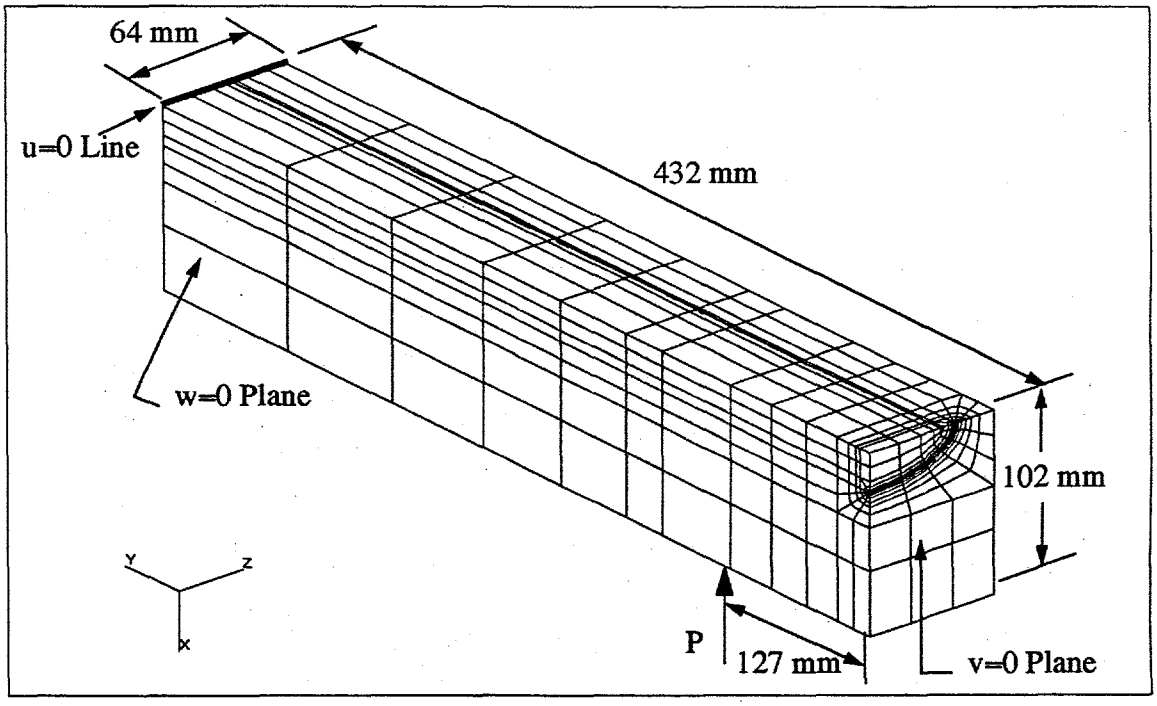

FIGURE 1. Quarter Symmetry Finite Element Model for Unclad WPS Model.

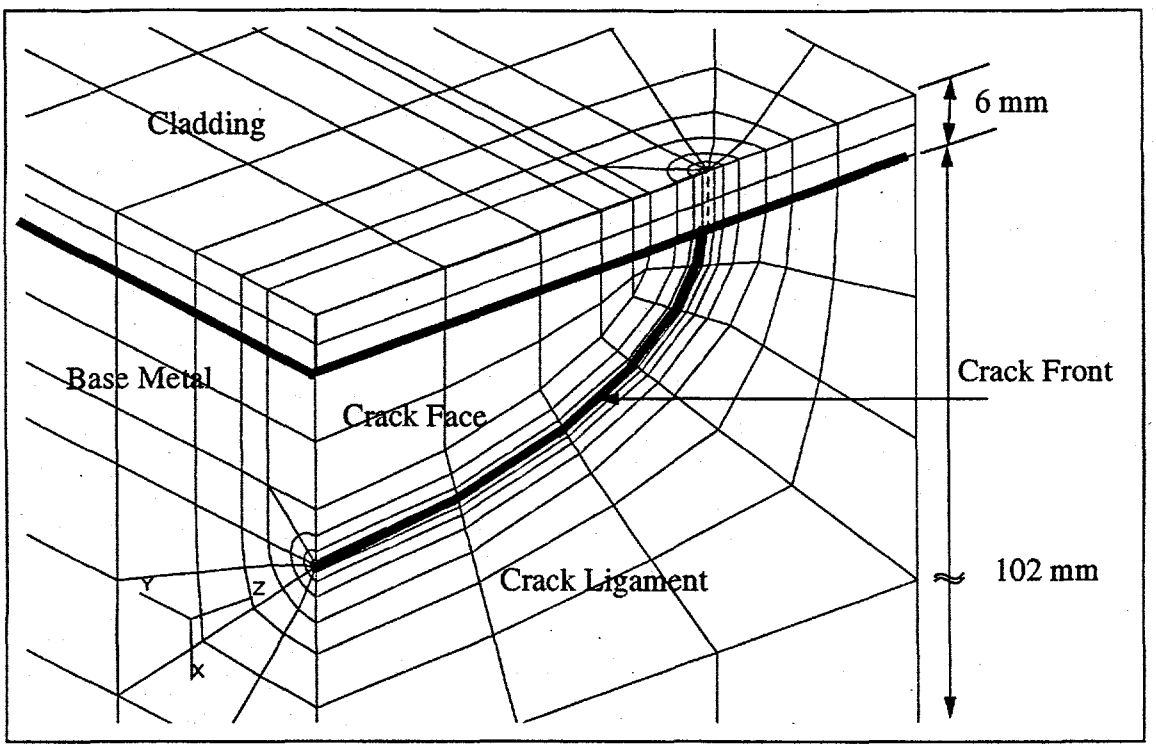

FIGURE 2. Crack Front on Quarter Symmetry Finite Element Model for Clad Model.

the unclad model. The modeled flaw was a semi-elliptical flaw 80 mm long and 21 mm deep. Figure 2 also shows the details of the modeled crack front.

All the elements of the finite element model were 20-noded hexahedron three-dimensional solid elements with the exception of the degenerate hexahedron elements along the crack front. All elements used the 2x2x2 Gaussian integration scheme. The finite element mesh along the crack front was created such that elements had a $1/\sqrt{r}$ singularity (i.e., quarter-point elements). Preliminary analyses using different flaw sizes revealed that the difference between the stress intensity factors obtained with a flaw 21 mm deep and those obtained using a flaw 19 mm deep was less than five percent for the unclad WPS specimens. Hence, the 21mm selected flaw depth was considered appropriate for this analysis since it would provide reasonable stress intensity factors. The flaw region was modelled using six elements along the crack front, four rings of elements around the crack front, and six $1/\sqrt{r}$ singularity elements surrounding the crack tip. A comparison analysis using nine elements along the crack front, six rings of elements around the crack front, and six $1/\sqrt{r}$ singularity elements surrounding the crack tip resulted in less than one percent difference in the stress intensity factors on an unclad WPS finite element model. Consequently the simpler crack front finite element model was used.

To enforce the quarter symmetry of the finite element model, two of the vertical faces had the normal displacements (v and w) set equal to zero. On the flaw plane, including the cladding but not the crack face region, the global Y displacement (v) was set equal to zero. No displacement boundary conditions were imposed on the crack face. Along the beam's length centerline, the global Z displacement (w) was set equal to zero. These faces are labeled v=0 and w=0 in Figure 1. To simulate the four-point beam reaction loads, the finite element model was supported across the top edge, 432 mm from the flaw plane, by setting the global X displacement (u) equal to zero. A point load was applied 127 mm from the flaw plane along the bottom of the finite element model. Constraint equations were used in

the finite element analysis program to ensure that the displacements in the global X direction (u) for the nodes along the loading edge were equal to the node displacement where the point load was applied. To simulate the quarter symmetry of the loading, the magnitude of the point load was one-quarter of the actual load applied.

MATERIAL PROPERTIES

The base metal on the WPS test block was modeled using A508 Class 2 low alloy steel properties. With one exception, the cladding was modeled using 3-wire 308-309 stainless steel cladding (SS30X) properties. The remaining analysis was performed using Inconel EN82 cladding properties. Material properties at test temperatures (i.e., −129°C, −18°C, and 149°C) were obtained as part of the WPS test program. Material properties at high temperatures (from 149°C up to 677°C) were obtained from a previously established high temperature material properties database [4]. Table 1 shows the material properties for cladding and base metal used in this analysis. Poisson's ratio, ν, was assumed to be 0.3 for all materials and temperatures.

TABLE 1. Material properties used in finite element analysis.

	SS30X Clad			EN82 Clad			A508 Cl2 Base Metal			
Temp. (C)	Sy (MPa)	E (GPa)	$\alpha_{(mean)}$ (E-06 1/C)	Sy (MPa)	E (GPa)	$\alpha_{(mean)}$ (E-06 1/C)	Sy (MPa)	E (GPa)	$\alpha_{(mean)}$ (E-06 1/C)	Source Ref. #
-129	391	301	18.05	568	284	14.90	710	351	10.94	2
-18	363	279	18.62	447	223	15.40	558	276	11.54	2
149	315	262	19.46	403	201	16.15	503	249	12.44	2
260	197	178	20.03	334	174	16.64	382	189	13.05	4
399	166	167	20.73	320	164	17.27	346	178	13.80	4
538	135	155	21.44	307	154	17.89	310	167	14.55	4
677	103	143	22.14	293	145	18.51	274	157	15.31	4

Figure 3 shows engineering stress-strain curves for the three materials at 149°C. Stress-strain curves at other temperatures followed similar trends.

In this analysis the reference temperature (i.e., stress free temperature) was assumed to be 621°C. This provided the means to obtain an estimate of the residual stresses on the cladding which was judged to be reasonable. Kinematic strain hardening plasticity model was selected to represent the base metal and cladding material responses.

The material properties of the high strength A533 steel extension arms were assumed to be elastic and constant for the proposed temperature range. The Modulus of Elasticity, E, used was 210 MPa. The thermal expansion coefficient, $\alpha_{(mean)}$, was 8.3×10^{-6} °C^{-1}.

To assist the model construction, cladding elements were created on the extension arms. But, since there was no cladding on the extension arms of the WPS specimen, the cladding elements over the extension arms were assumed to be linear-elastic and very flexible; the Modulus of Elasticity used was 7 KPa. No thermal expansion was allowed for these elements.

METHODOLOGY FOR COMPUTING STRESS INTENSITY FACTORS

Since the experiments involved loading, unloading, and reloading, J-integral calculations were valid for only the initial loading. Thereafter, due to changes in the ratios of the principal stresses, the correspondence between deformation theory and flow theory became nonexistent. Consequently, approximations were needed to estimate the crack driving force of the test specimens after unloading occurred.

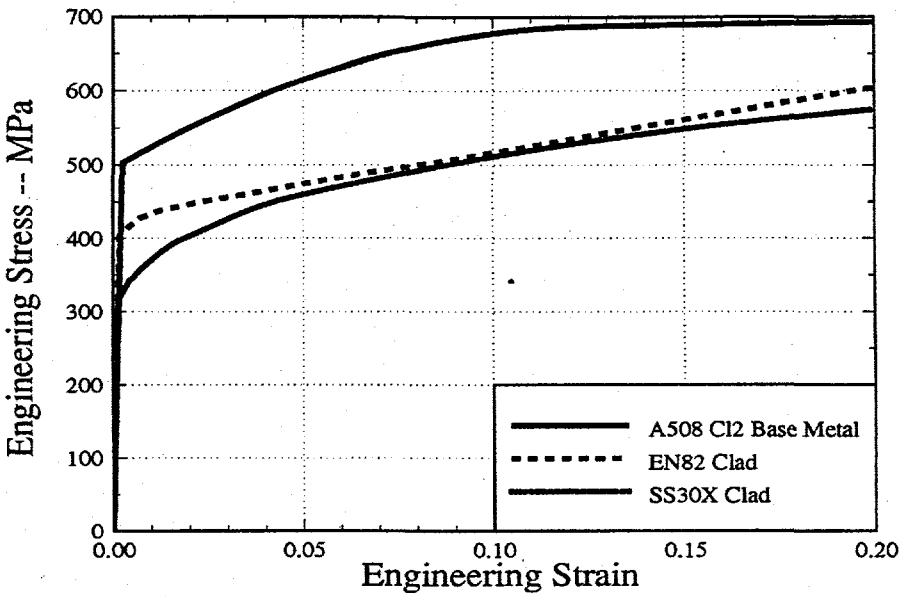

FIGURE 3. Engineering Stress-Strain Curves Used in Finite Element Analysis for Cladding and Base Metal Materials at 149°C.

An in-house linear-elastic fracture mechanics code was used to calculate elastic stress intensity factors, K_I, along the crack front on the WPS finite element model. K_I was calculated using the crack front element gauss point stresses [5]. K_{eff}, the plane strain plastic zone corrected value of K_I [6], was calculated using the following equation:

$$K_{eff} = \frac{K_I}{\sqrt{1 - \frac{K_I^2}{6\pi a S_y^2}}} \qquad (1)$$

where *a* is the flaw depth, and *Sy* is the yield stress at the WPS temperature.

An in-house elastic-plastic fracture mechanics code was used to calculate the energy release rate, G, along the crack front on the WPS finite element model. G was calculated using the virtual crack extension method [7][8]. G is equivalent to J, provided that path independence is demonstrated [9]. Path independence means that the energy release rate is nearly identical for different paths around the crack tip on a partition. A partition is defined as a surface that is topologically normal to the crack front containing either corner-nodes or mid-nodes of a crack front element. A path is roughly analogous to a J-integral contour around the crack tip. $K_I(J)$, the elastic plastic stress intensity factor was calculated using the following equation:

$$K_I(J) = \sqrt{E'G} = \sqrt{E'J} \qquad (2)$$

given that G is path independent, and where

$$E' = \frac{E}{1-\upsilon^2} \tag{3}$$

for plane strain conditions, where E is the Modulus of Elasticity and ν is Poisson's ratio.

The WPS finite element models used for this analysis had 13 partitions (i.e., six elements) along the crack front. Seven paths were used for partitions passing through corner-nodes and six paths were used for partitions passing through mid-nodes. The energy release rate calculation was performed in a partition-by-partition fashion, with each partition treated as a 2D plane.

WPS EXPERIMENTS

Displacement Matching

Figure 4 shows that the crack mouth opening displacement for the clad and unclad WPS beam experiments matches those obtained from the finite element models. Thus, the modeling efforts were considered to be accurate. The presence of cladding on the WPS model caused a reduction of the crack mouth opening displacements when compared to the unclad model. This suggests a significant cladding benefit.

Unclad Beam Results

Table 2 shows various estimates of the crack driving force for six of the WPS tests.

TABLE 2. Stress intensity factors for several unclad WPS beams.

Spec. ID	WPS Load (kips)	WPS Load (KN)	K_I MPa$\sqrt{m}$	K_{eff} MPa$\sqrt{m}$	$K_I(J)$ MPa$\sqrt{m}$	% Diff. between K_{eff} & $K_I(J)$
U01	148.9	662	87	90	89	-1.6
U02	149.3	664	87	90	89	-1.2
U13	175.1	779	102	108	110	2.5
U17	176.7	786	103	109	112	3.1
U27	192.1	854	112	119	130	9.1
U19	193.3	860	112	120	133	10.6

This table shows minimum and maximum stress intensity factors for three representative WPS load values. These stress intensity factors bound the results of the remaining samples. K_{eff} results were up to 10% lower than the $K_I(J)$; the larger difference occurring at the higher WPS loads. A comparison between the K_I from this analysis and the K_I calculated using the Newman-Raju elastic solution [10] showed good agreement even at the maximum load. Both K_I values were 112 MPa$\sqrt{m}$ at the deepest point of the flaw.

In addition, path independence was demonstrated for this model. Figure 5 shows that, for a given load step and partition, the energy release rate, G, values are nearly identical for two different paths around the crack tip.

Clad Beam Stress Relieving and Cooldown Process

Due to the higher coefficient of linear expansion of the cladding compared to that of the base metal, cooling from the stress relief temperature to room temperature caused residual stresses in the cladding and in the neighboring base metal. The residual stresses were tensile in the cladding and compressive in the neighboring base metal.

At room temperature the thermally induced tensile stresses in the cladding were higher in the SS30X cladding model than in the EN82 cladding model. This was due to the larger

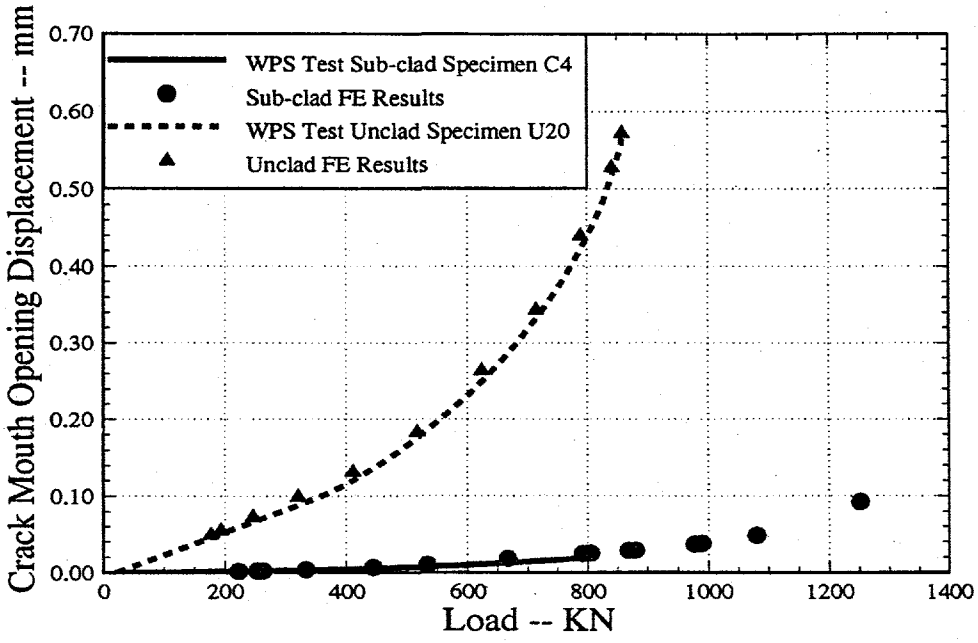

FIGURE 4. Crack Mouth Opening Displacement for Clad and Unclad Tests and Finite Element (FE) Results.

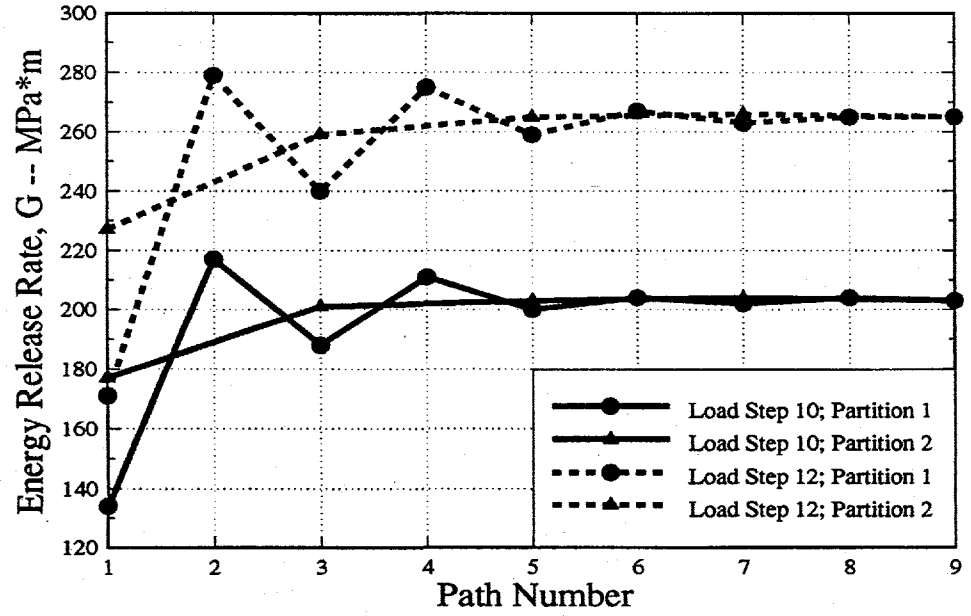

FIGURE 5. Variation of the Energy Release Rate, G, by Path for a Given Partition to Demonstrate Path Independence of G Results on Finite Element Model. (Note: Step 10 and 12 denote increasing load steps used in the analysis.)

coefficient of thermal expansion for the SS30X when compared to the EN82. As a result, the SS30X cladding (which has a yield stress of 328 MPa) yielded almost completely due to cooling following stress relief. On the other hand, the EN82 cladding (which has a yield stress of 430 MPa) yielded only near the free surface. As a consequence of the lower yield

strength of the SS30X cladding, the compressive stresses in the neighboring base metal were lower than those associated with the EN82 cladding. Hence the expectation was that the fracture loads would be lowest for the unclad beams, somewhat higher for the SS30X clad beams, and highest for the EN82 clad beams.

Figure 6 shows the effect of cladding residual stresses at the deepest point of the flaw, and the edge of the flaw at the clad-base metal interface. As one might expect, the compressive stresses in the base metal are more significant at the edge of the flaw (dashed line) than at the depth (solid line). This effect diminishes with increasing load.

Effectiveness of Cladding Regarding Crack Driving Force

Figure 7 shows $K_I(J)$ at the deepest point of the flaw as a function of applied WPS load for a surface flaw and its Newman-Raju elastic solution, for the SS30X clad beam, and for the EN82 clad beam at 149°C. The results for the surface flaw serve to verify the modeling and to indicate the extent of the influence of plasticity. When subjected to the applied bending stress, $K_I(J)$ was at first dominated by crack closing force due to tensile residual stresses in the cladding. Upon further loading, the cladding completely yielded in tension and could supply no additional closing force. The cladding ligament causes the initial response to resemble that of a buried defect. The strength of the EN82 cladding was higher than the SS30X, and therefore caused the greatest departure from the surface flaw response as yielding in the cladding became more pronounced.

Figure 8 shows $K_I(J)$ at the deepest point of the flaw as a function of applied load for the SS30X clad model at three different temperatures. These curves show that as temperature decreases and cladding strength increases, the crack driving force is more greatly diminished in a manner similar to that shown in Figure 7.

Next, the responses of the unclad and sub-clad flaws are compared to show how the cladding effect can be modeled with elastic solutions. Figure 9 shows the effect of cladding on the crack driving force as a function of applied load. When the cladding has completely yielded, the sub-clad flaw response becomes offset below the unclad flaw

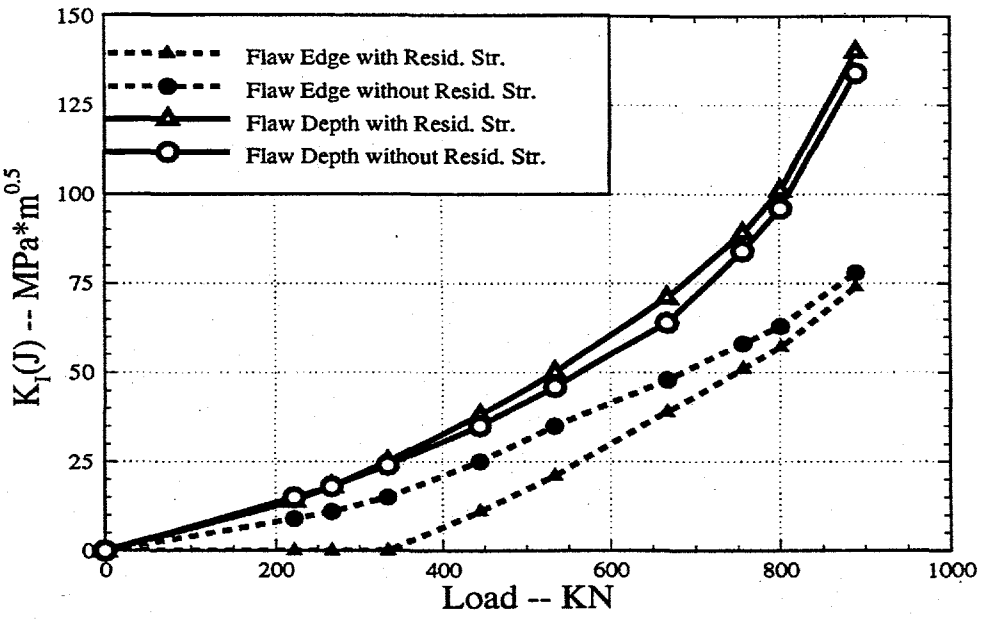

FIGURE 6. Effect of Cladding Residual Stresses on $K_I(J)$ at Depth and Edge of Sub-clad Flaw.

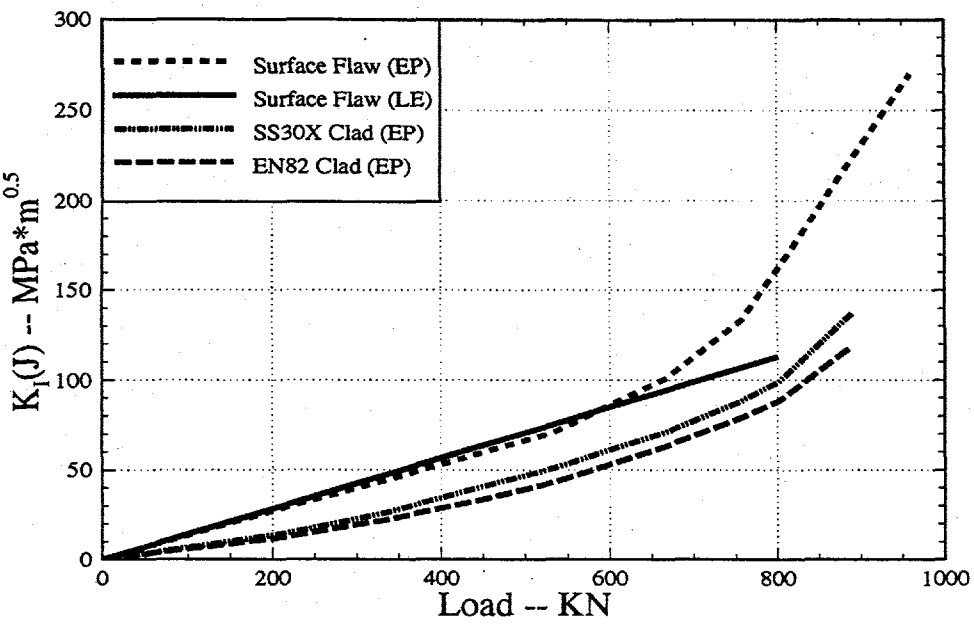

FIGURE 7. Stress Intensity Factors versus Applied Load for Three Clad Conditions (Note: EP = Elastic-Plastic Analysis; LE = Linear Elastic Analysis)

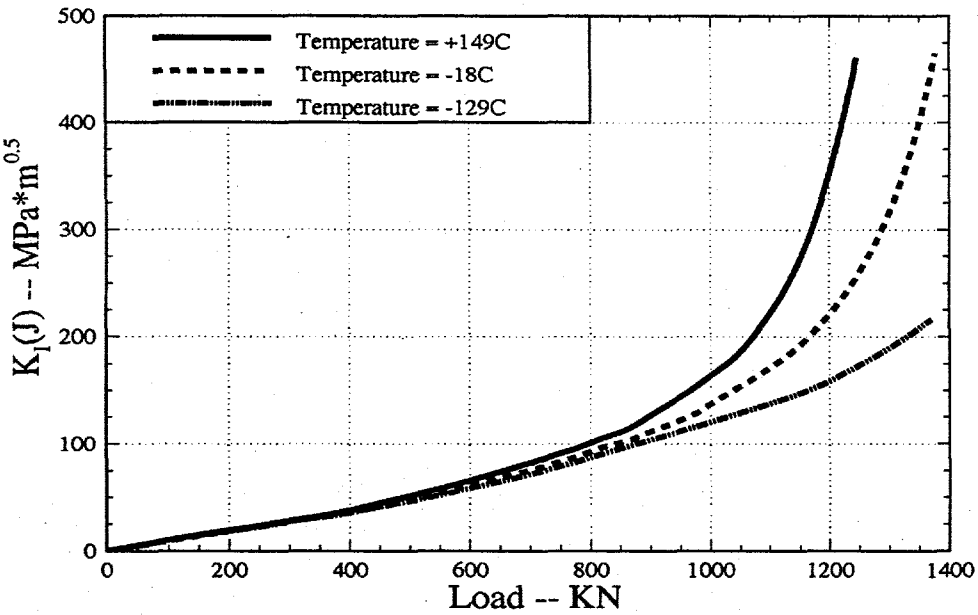

FIGURE 8. Stress Intensity Factors versus Applied Load for SS30X Clad Model at Three Temperatures.

response by a constant value. This suggests that if $K_I(J)$ for the unclad flaw is known, using for example the Newman-Raju elastic solution with a plastic zone correction, $K_I(J)$ for the sub-clad flaw can be obtained by subtracting some crack closure force $K_I(J)$ value due to the presence of the cladding.

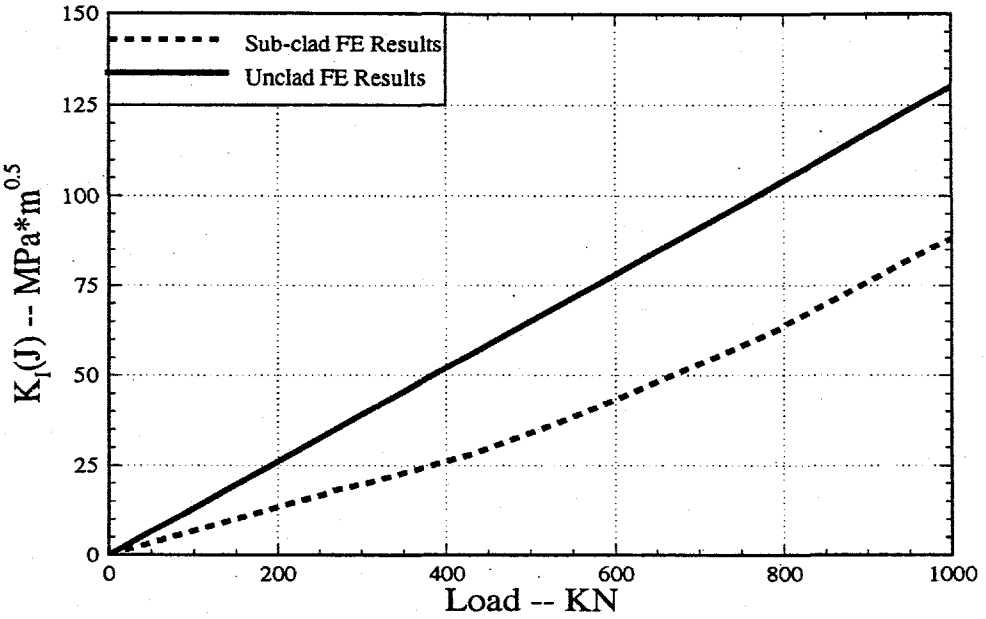

FIGURE 9. Effect of Cladding on Warm Prestress Beam Crack Driving Force From Finite Element (FE) Results.

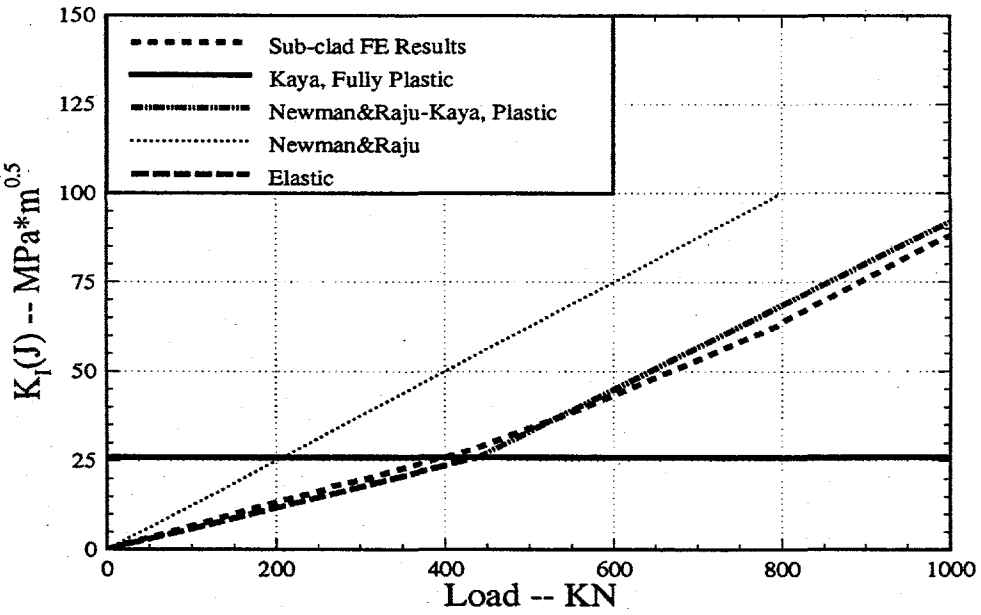

FIGURE 10. Elastic Estimates of the Effects of Cladding on Warm Prestress Beam Crack Driving Force.

Figure 10 shows a combination of elastic solutions that approximate the trends lines from Figure 9. The approximation to the cladding crack closure forces were determined from existing elastic solutions. The Kaya-Erdogan [11] solution for an edge crack loaded by opposing forces at its free edge was used to represent the fully plastic cladding crack closure force estimate. The SS30X yield stress was used to calculate the force for this

"fully plastic" estimate. The flaw depth was set equal to that of the surface elliptical flaw. The fully yielded cladding result was obtained by subtracting the "fully plastic" Kaya-Erdogan solution at yield load from the plastic zone corrected Newman-Raju solution for the surface flaw. This estimate was discontinued at the "fully plastic" estimate, and an elastic estimate was obtained by extending a straight line from this point to the origin. Figure 10 suggests that the combination of these solutions provides a reasonable estimate of the elastic-plastic sub-clad flaw response.

LOCALLY INTENSIFIED STRAIN AGEING EMBRITTLEMENT

Mylonas and Rockey [12] and others, and most recently Dawes [13] have commented on the occurrence of abnormally low toughness near welded over notches. Apparently the thermal strains associated with welding are amplified by the presence of the notch at temperatures in the strain ageing regime, resulting in degraded toughness. One of the more dramatic examples of this locally intensified strain ageing embrittlement was the 1943 complete amidships fracture of the new tanker SS Schenectady while tied up at the dock at night in calm weather [13]. On a less grand scale, the manufacturing procedure for the sub-clad flaw specimens provided all the key ingredients for locally intensified strain ageing embrittlement as noted in Appendix A. Figure 11 shows $K_I(J)$ for sub-clad and surface flawed WPS beams tested at -129°C without prior WPS. The variability of $K_I(J)$ for the sub-clad specimens indicates toughness degradation.

The trend lines in Figure 11 are those seen in Figure 9 for sub-clad and unclad flawed beams. Perhaps the most clear indication of locally intensified strain ageing embrittlement is provided by comparing the filled and open circles. The filled circle represents a sub-clad flawed specimen which had the cladding removed prior to testing. The open circles represent surface flaw specimens. The toughness degradation due to welding over the flaw appears to be significant. However, the sparseness of the data for the unclad case precludes their quantitative assessment. The x's represent sub-clad flawed beams with the same

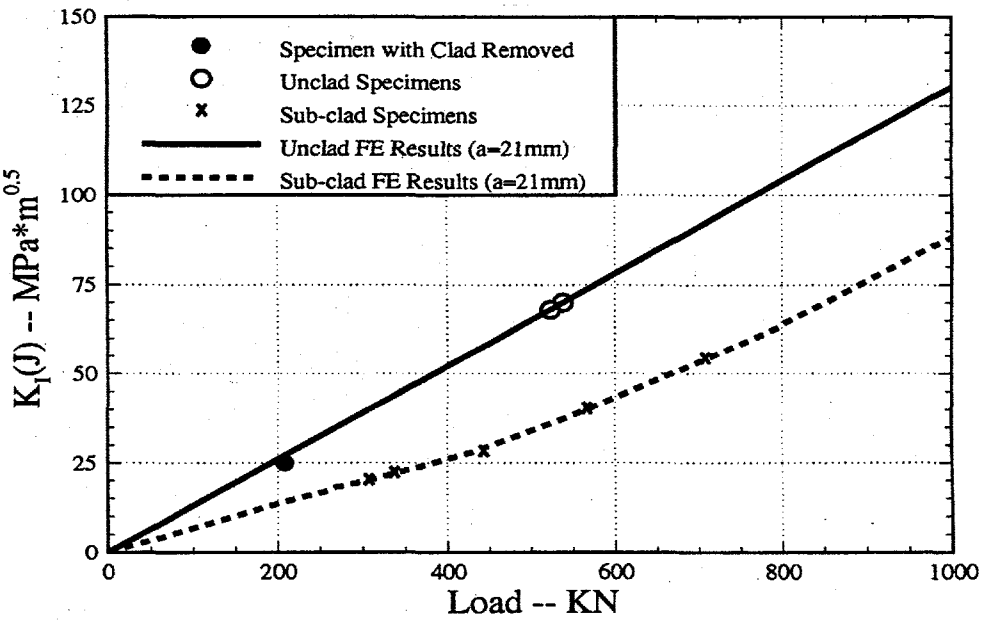

FIGURE 11. Effect of Locally Intensified Strain Aging Embrittlement on Flawed WPS Beams at −129°C Without Prior Warm Prestressing.

nominal flaw size which were expected to carry far more load at failure than their surface flawed counterparts. That was the case in only one instance, and in that case the apparent toughness was still degraded. Data presented by Macdonald, et al. [2] showed that the WPS evolution was effective in removing the toughness distinction between the sub-clad and unclad flawed beams as the sub-clad beams behaved like the unclad beams as long as the cladding remained intact.

COMPARISON WITH OTHER INVESTIGATORS

The conclusions reached in this report are in agreement with those presented by Miyazaki, et al. [14]. Although their work was based in terms of the stress triaxiality near the crack tip, they predicted that a clad material with a higher yield stress enhances the fracture toughness of a base material. Similar behavior was observed for the EN82 cladding model when compared to the SS30X cladding model, and for the –129°C SS30X cladding model when compared to the 149°C SS30X cladding model. In both of these cases the applied stress intensity factor is less for a given load, which would translate to an enhancement of the fracture toughness.

The overall behavior of the structure was well modeled and it follows the prediction by Keeney, et al. [15] (i.e., the effect of the clad material on an underclad flaw is to suppress crack opening). This is also supported by similar work performed by Electricité de France and analyzed by Keeney [16]. Although differences in finite element models, material properties, and boundary conditions prevent a direct comparison of the data and results, the analysis process used in this report agrees with that presented by Keeney.

Other work dealing with sub-clad flawed beams was also reviewed for their potential applicability to this work. Reference 17 included an assessment of cladding effects on finite element cracks due only to a pressurized thermal shock. Although thermal effects were considered in this analysis, they were not the only source of loading. Reference 18 included a 2D analysis used to determine fracture toughness estimates using the η-factor method. In addition, the Reference 18 finite element model was refined enough to provide information about the crack tip stress triaxiality using the J-Q Methodology. Unfortunately the model in this work was intended to generate stress intensity factors only and constraint was not considered. Therefore, direct comparison with Reference 18 is not possible. Finally, Reference 19 included the evaluation of stress intensity factors for semi-elliptical flaws using stress intensity factor influence coefficients. Although a number of models with different geometric ratios were presented, a direct comparison with the finite element model used in this work was not possible. The geometric ratios of the finite element model used in this work were not explicitly presented in Reference 19.

SUMMARY

Three-dimensional elastic-plastic finite element techniques were applied to detailed linear-elastic and elastic-plastic fracture mechanics of WPS experiments using clad and unclad beams in four-point bending. Comparison of crack mouth opening displacements showed good agreement between the experiments and analyses which indicate the adequacy of the finite element models. Comparison of linear-elastic with the Newman-Raju approximation also revealed good agreement. Comparison of K_{eff} and $K_I(J)$ also showed the adequacy of the finite element model and the computational techniques.

CONCLUSIONS

When modeling the stress relieving process, the cooldown to room temperature caused metal contraction which induced tensile residual stresses on the cladding and compressive residual stresses on the neighboring base metal due to a greater coefficient of thermal expansion for the cladding than for the base metal. Larger cooldowns created larger tensile residual stresses on the cladding and the compressive residual stresses on the neighboring base metal. The influence of the residual stresses on the crack driving force diminished as the distance from the clad-base metal interface increased. During loading, $K_I(J)$ increased due to the applied tensile bending stress. At first, however, $K_I(J)$ was dominated by crack closing force due to tensile residual stresses in the cladding. Further loading caused the cladding to yield completely and not supply additional closing force. The trends of $K_I(J)$ versus applied load curves were below the unclad $K_I(J)$ curve, with the EN82 cladding curve the lowest of the two. Similarly, $K_I(J)$ versus load curves as a function of temperature followed the expected trend. Lower temperatures experienced reduced $K_I(J)$ values supporting the influence of increased lower yield strength at lower temperatures.

A combination of elastic stress intensity factor solutions was used to approximate the effect of cladding in reducing the crack driving force along the flaw. This approximation was quite in keeping with the 3D elastic-plastic finite element solution for the sub-clad flaw.

Finally, a number of sub-clad flaw specimens not subjected to warm prestressing were thought to have suffered toughness degradation caused by locally intensified strain ageing embrittlement due to welding over the preexisting flaw.

ACKNOWLEDGMENTS

The authors wish to acknowledge the following individuals for their assistance with this work: P.D. Vozzola and W.W. Wilkening for their input to and review of finite element models and techniques used in this analysis; G.T. Embley and P.D. Smith for providing insight into the WPS phenomena; and J.W. Wuthrich for his help with the details of the WPS Test Program.

REFERENCES

1 Chell, G.G., Haigh, J.R., and Vitek, V., "A Theory of Warm Prestressing: Experimental Validation and the Implications for Elastic Plastic Failure Criteria", CERL Report No. RD/L/N 63/79, 1979.

2 Macdonald, B.D., et al., "Analysis of Warm Prestress Data", Fatigue and Fracture Mechanics: 27th Volume, ASTM STP 1296, 1995.

3 PATRAN Version 2.5 and P3 Version 1.4 Users Manual, MacNeal-Schwendler Corporation, PDA Engineering, 1994.

4 Wilkening, W.W. and Snow, J.L., "Analysis of Welding-Induced Residual Stresses with the ADINA System", Computers and Structures, Vol. 47, No. 4/5, 1993, pp 767-786.

5 Irwin, G.R., "Analysis of Stresses and Strains near the End of a Crack Traversing a Plate", Journal of Applied Mechanics, Vol. 24, 1957, pp. 361-364.

6 Irwin, G.R., "Plastic Zone Near a Crack and Fracture Toughness", Sagamore Research Conference Proceedings, Vol. 4, 1961.

7 deLorenzi H.G., "On the Energy Release Rate and the J-Integral of 3-D Crack Configurations", International Journal of Fracture, Vol. 19, 1982, pp. 183-193.

8 deLorenzi H.G., "Energy Release Rate Calculations by the Finite Element Method", Engineering Fracture Mechanics, Vol. 21, 1985, pp.129-143.

9 Rice J.R., "A Path Independent Integral and the Approximate Analysis of Strain Concentrations by Notches and Cracks", Journal of Applied Mechanics, Vol. 35, 1968, pp. 379-386.

10 Newman, J.C. and Raju, I.S., "Analysis of Surface Cracks in Finite Plates Under Tension or Bending Loads", NASA Technical Paper 1578, December 1979.

11 Tada, H., Paris, P. C., and Irwin, G.R., The Stress Analysis of Cracks Handbook, 2nd Edition, Paris Production Incorporated (and Del Research Corporation), 1985, pp. 2.25.

12 Mylonas, C., and Rockey, K.C., "Exhaustion of Ductility by Hot Straining —An Explanation of Fracture Initiation Close to Welds", Welding Journal, Vol.40, No. 7, Research Supplement, 1961, pp 306s-310s.

13 Dawes, M.G., "Significance of Locally Intensified Strain Ageing to the Fracture Toughness of Welded Steel Structures", Fracture Mechanics, 26th Volume, ASTM STP 1256, 1995.

14 Miyazaki, N., Ikeda, T., and Ochi, K., "Constraint Effects of Clad on Underclad Crack", Fatigue and Fracture Mechanics in Pressure Vessel and Piping, PVP-Vol. 304, ASME, 1995, pp. 313-318.

15 Keeney, J.A., Bass, B.R., and Pennell, W.E., "Evaluation of the Effects of Irradiated Cladding on the Behavior of Shallow Flaws Subjected to Pressurized Thermal Shock Loading", Transactions of the 11th International Conference on Structural Mechanics in Reactor Technology, Vol. G, 1991, pp. 195-200.

16 Keeney, J.A., "Cleavage Fracture Analysis of the French Clad Beam Experiments", ORNL/NRC/LTR-94/24, Oak Ridge National Laboratory, October 1994.

17 Keeney, J.A., Bass, B.R., Sievers, J., and Xiaoming, L., "Analysis of a Pressurized Thermal Shock Experiment for Assessing Cladding Effects on Finite Element Cracks", Fatigue, Flaw Evaluation and Leak Before Break Assessments, PVP-Vol. 280, ASME, 1994, pp. 45-50.

18 Keeney, J.A., Bass, B.R., and McAfee, W.J., "Fracture Analysis of Full Thickness Clad Beams Specimens", Fatigue and Fracture Mechanics: 27th Volume, ASTM STP 1296, 1995.

19 Keeney, J.A. and Bryson, J.W., "Stress Intensity Factor Influence Coefficients for Semielliptical Inner Surface Flaws in Clad Pressure Vessels", Fracture Mechanics: 26th Volume, ASTM STP 1256, 1995.

Appendix A

SUMMARY OF WARM PRESTRESSING EXPERIMENTS

Introduction

The unclad warm-prestress (WPS) experimental program consisted of a total of 38 tests in two groups. The first group was a control matrix of 6 specimens tested under isothermal conditions at three different temperatures, –129°C, –73°C, and –18°C. These tests were conducted to provide a baseline for evaluation of the fracture toughness. The second group, the WPS tests, consisted of 32 tests. Three types of WPS load/temperature scenarios were used. These are shown schematically in Figure A1 and were defined as Load-Unload-Cool-Fracture (LUCF), Load-Cool-Unload-Fracture (LCUF), and Load-Linear Cool and Unload-Fracture (LIN).Data for the unclad WPS tests is shown in Table A1.

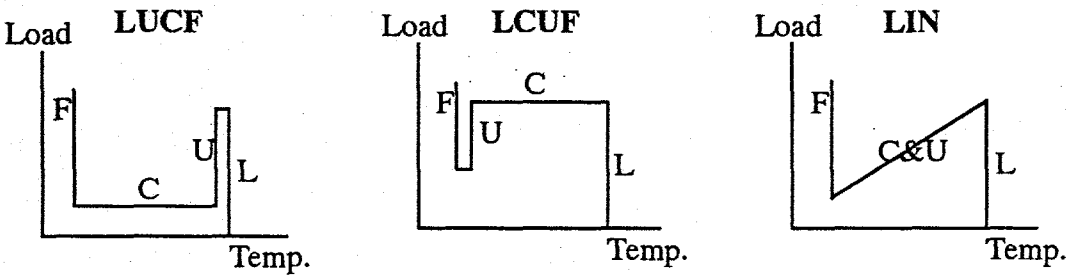

FIGURE A1. WPS Load/Temperature Scenarios.

TABLE A1. WPS test matrix and results for unclad flawed beams.

Specimen	WPS Load (kips)[a]	Minimum Load (kips)[a]	Fracture Temp. (°F)[b]	Fracture Load (kips)[a]
Load - Unload - Cool - Fracture				
U01	148.9	37.5	–200	161.4
U29	175.8	115.4	–200	195.1
U22	192.6	78.7	–200	222.2
U08	150.4	115.9	–100	183.1
U14	176.1	78.3	–100	219.9
U20	193.0	39.7	–100	228.8
U06	150.4	78.5	0	252.8
U12	176.2	40.1	0	236.3
U27	192.1	115.4	0	231.7

TABLE A1. WPS test matrix and results for unclad flawed beams.

Specimen	WPS Load (kips)[a]	Minimum Load (kips)[a]	Fracture Temp. (°F)[b]	Fracture Load (kips)[a]
Load - Cool - Unload - Fracture				
U07	150.2	115.4	−200	171.9
U13	175.1	79.1	−200	212.3
U19	193.3	38.8	−200	216.8
U05	149.5	77.9	−100	175.2
U11	175.9	39.0	−100	208.8
U26	193.2	114.8	−100	237.5
U03	157.0	39.0	0	224.0
U18	175.6	114.8	0	206.1
U24	192.5	78.4	0	221.5
Load - Linearly Cool and Unload - Fracture				
U04	149.1	78.9	−200	172.7
U10	176.1	40.4	−200	161.2
U25	193.1	114.9	−200	231.9
U02	149.3	39.5	−100	200.0
U17	176.7	114.4	−100	207.3
U23	193.0	76.4	−100	217.7
U09	149.7	115.8	0	173.4
U15	175.9	77.5	0	224.7
U28	192.4	37.5	0	217.1

a. 1 kip = 1000 lbf; 1 lbf = 4.448 N
b. °C = (°F-32)/1.8

The sub-clad WPS experimental program consisted of a total of 8 tests. WPS beams with sub-clad flaws were similarly tested with similar load/temperature scenarios. The data is shown in Table A2.

TABLE A2. WPS test matrix and results for sub-clad flawed beams.

Specimen	WPS Load (kips)[a]	Minimum Load (kips)[a]	Fracture Temp. (°F)[b]	Fracture Load (kips)[a]
Load - Unload -Cool - Fracture				
C2	178.0	59.0	0	242.8
C4	180.0	120.0	0	281.4
C1	179.0	58.0	−200	193.3
C3	179.0	120.0	−200	220.6
Load - Cool - Unload - Fracture				
C6	181.0	57.0	0	222.4
C8	181.0	120.0	0	219.8
C5	180.0	60.0	−200	228.4
C7	180.0	120.0	−200	224.6

a. 1 kip = 1000 lbf; 1 lbf = 4.448 N
b. °C = (°F-32)/1.8

Specimen Fabrication

The unclad test specimens were beams 864 mm long, 102 mm high, and 127 mm wide. They were of a composite design in which only the test section was fabricated from pedigreed material. The dimensions and general layout of the test sections are shown in Figure A2. Blanks for the test sections were taken from an ASTM A508 Class 2 steel pressure vessel cylinder.

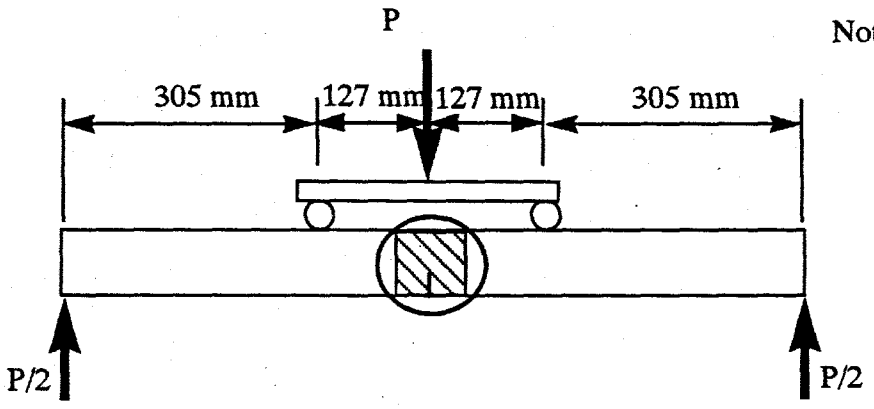

FIGURE A2. Schematic of WPS Test Beams

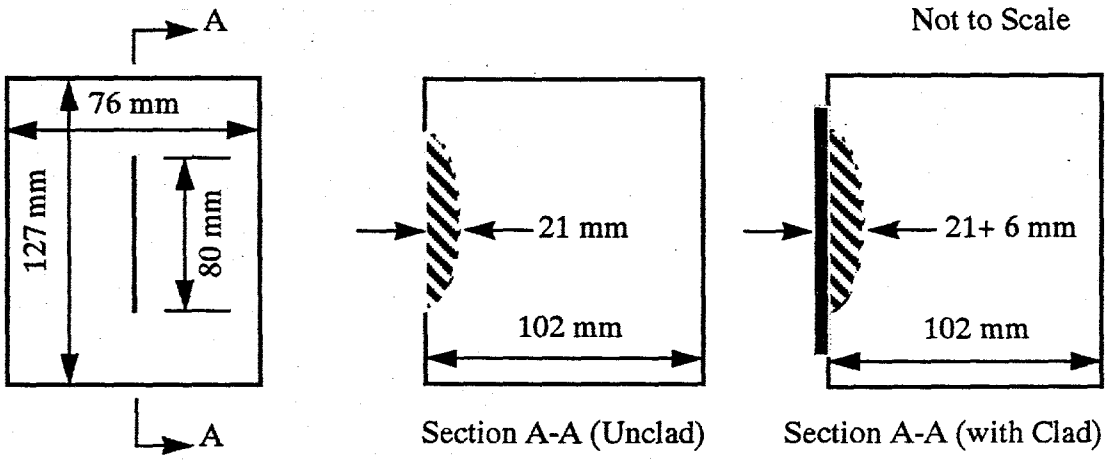

FIGURE A3. WPS Test Sections Schematic for Unclad and Sub-clad Beams

The unclad blanks were machined into test sections with final dimensions as shown in Figure A3. The flaw was ram electron discharge machined into the top surface of the test section in the shape of a semi-ellipse 76 mm long and 19 mm deep prior to fatigue pre-cracking. After machining, the test sections were post-weld-heat-treated in Argon at 621°C for 30 hours. This heat treatment was added to simulate the processing environment of the later sub-clad beams. Reusable A533 steel beam extension arms were electron-beam welded to the ends of the test section to form the full beam configuration. After electron beam welding the extension arms onto the test section, final machining was performed to remove the electron beam weld buildup.

The clad specimens were of the same geometry as the unclad with the exception of an additional 6 mm layer of cladding which was deposited after fatigue pre-cracking. The cladding was a either 3-wire 308-309 stainless steel (SS30X) or Inconel EN82 weld deposit.

Instrumentation

Each beam was instrumented to measure crack mouth-opening-displacement, surface strain, and temperature. Stroke, or test machine actuator movement, was measured

through the test machine controller to obtain an indication of load-line displacement for the beam. On the isothermal tests, a linearly variable differential transducer was mounted to measure the load line displacement directly. However, for the WPS tests, the entire beam was fully enclosed in an environmental chamber, so direct measurements of load line displacement could not be made. The clad beams included additional instrumentation to track cladding deformation.

Temperatures were measured using contact thermocouples. Eight thermocouples were mounted on the surface of the test section. An additional thermocouple was inserted into the center of the test section through a side hole. This thermocouple made contact with the material near the center of the block and was used for control of the experiment.

Test Procedure

The procedures contained in ASTM Standard Test Method for Plane-Strain Fracture Toughness of Metallic Materials (E 399) were used as guidelines for these tests, although they do not apply explicitly to the semi-elliptic flaw configuration. After the specimen was instrumented, it was mounted in a four-point bend test fixture, as shown schematically in Figure A2. The specimens were fatigue precracked at room temperature using change-in-compliance measurements to determine the amount of crack growth. Development tests were performed to establish the final test procedures to yield about 2 mm of crack growth needed to obtain a final flaw about 80 mm long and 21 mm deep. As noted earlier, the 6 mm layer of cladding was deposited after fatigue pre-cracking the clad beams.

After fatigue pre-cracking, in situ instrumentation checks were performed, and the specimen was prepared for the fracture portion of the test. For the control matrix tests, the specimen was cooled to the test temperature and held for a minimum of 20 minutes to establish isothermal conditions in the test section. The specimen was then loaded to failure.

The WPS tests varied from this procedure because of additional equipment requirements. After fatigue pre-cracking, electric heaters were mounted on the specimen, a liquid nitrogen manifold was installed, and an environmental chamber that completely enclosed the specimen was put in place. The specimen was aligned and pre-loaded to 22-kN. Holding the load constant, the specimen was heated to the WPS temperature of 149°C. For a Load-Unload-Cool-Fracture test, a stable WPS temperature was established and the specified load-unload cycle was applied at a rate of 0.003 Hz using a test machine generated displacement haversine function. Using load-control, the specimen was cooled to the fracture temperature, and the load increased until fracture occurred. For a Load-Cool-Unload-Fracture test, the specimen was loaded using a load-control ramp function. The load was held constant during cool-down to the fracture temperature. The load was then lowered to the pre-load value, and the load increased until fracture occurred. For the Load-Linear Cool and Unload-Fracture test, the WPS and failure sequences of the test were the same as for the Load-Cool-Unload-Fracture. However, the Load-Linear Cool and Unload-Fracture test utilized a controller that maintained a linear relationship between the specimen temperature change and the applied load change.